Robert J. Lang
Lang Origami,
Alamo, CA 94507
e-mail: robert@langorigami.com

Spencer Magleby
Department of Mechanical Engineering,
Brigham Young University,
Provo, UT 84602
e-mail: magleby@byu.edu

Larry Howell
Department of Mechanical Engineering,
Brigham Young University,
Provo, UT 84602
e-mail: lhowell@byu.edu

Single Degree-of-Freedom Rigidly Foldable Cut Origami Flashers

We present the design for a family of deployable structures based on the origami flasher, which are rigidly foldable, i.e., foldable with revolute joints at the creases and planar rigid faces. By appropriate choice of sector angles and introduction of a cut, a single degree-of-freedom (DOF) mechanism is obtained. These structures may be used to realize highly compact deployable mechanisms. [DOI: 10.1115/1.4032102]

1 Introduction

Many patterns from the world of origami have application in the world of engineering, particularly in the area of deployable structures. Whenever there is a need for a mechanism to transform between a large, flat, sheetlike state (the "deployed" state) and a much smaller state ("stowed"), origami-based mechanisms can provide efficient solutions.

One origami mechanism that has received considerable attention over the years is the pattern called a "flasher," which was introduced and explored in the origami world by Palmer and Shafer [1]; they developed their concept from the twist-fold forms of Kawasaki (see, e.g., Ref. [2]). However, the concept had a long existence outside of the origami world. As noted by Guest and Pellegrino (see Ref. [3] and references therein), several authors have discovered and explored similar structures since the early 1960s and it is regularly rediscovered. Nojima [4] showed a variety of similar forms with varying degrees of helicity and rotational symmetry. For purposes of this work, we will refer to all of these patterns that are rotationally symmetric, roughly flat in the deployed state, roughly cylindrical in the stowed state, and deploy in a spiral pattern, as (generalized) *flashers*.

Most work has focused on the use of the flasher mechanism in concert with membranes, or at least, structures that have distributed flexibility [5,6]. While many flashers have been demonstrated from relatively stiff materials, the basic flasher mechanism and, to the best of our knowledge, all versions proposed and demonstrated to date are not *rigidly foldable*; they cannot be folded continuously from the stowed to the deployed state with rigid panels and pure revolute joints.

To get around this problem, several alternatives have been proposed and/or demonstrated that work with rigid panels. Guest and Pellegrino proposed a structure composed of separate panels joined by struts [7]. Zirbel et al. demonstrated a prototype solar array using a flasher structure with rigid panels and finite-width membrane hinges between the panels, in which the flexible membrane hinges provide the necessary additional compliance needed for deployment [8], albeit at the cost of introducing potentially undesirable additional DOF into the motion.

It is also potentially possible to add DOF by triangulating some fraction, perhaps all, of the quadrilateral panels to allow some amount of flexing across their diagonals. However, whether such an approach guarantees full reachability across the range of motion and the effects on the DOF of the mechanism remain open questions for that approach.

An additional challenge with using idealized flasher patterns in real-world engineering is the problem of thickness: idealized patterns assume zero (or negligible) thickness, but in real-world applications, the thickness of each panel is usually non-negligible. Finite thickness matters in two ways. First, it affects *metric foldability*: offsets and displacements of hinges from their idealized zero-thickness positions can affect the mechanics of folding or even prevent folding by turning a flexible mechanism into a locked structure. Second, it affects *injectivity*, or self-intersection: the layers of a thick structure can collide with each other even if the corresponding zero-thickness model does not self-intersect. Fortunately, recent work by Tachi [9] and Edmonson et al. [10] demonstrated effective techniques for adapting zero-thickness structures with non-negligible thickness panels, and such techniques are applicable here.

Self-intersection aside, the problem of metric foldability remains. In particular, for applications with rigid panels, it would be desirable to have a folding pattern that is rigidly foldable. Even better, it would be desirable for the folding motion to have a single DOF, so that there is one and only one path between the stowed and deployed states.

In this paper, we propose, describe, and analyze a member of the flasher family of mechanisms that meets both criteria: it is rigidly foldable with planar panels and pure revolute joints and transforms continuously from a fully flat state to a compact, cylindrical configuration with a single DOF. Like another well-known deployable structure, the Miura-ori [11], it is overconstrained according to the Kutzbach criteria, but by careful choice of angles in the design, we can realize a single DOF in the deployment motion; however, it is necessary to introduce a cut into the mechanism. Furthermore, there is a tuning parameter for the spacing between layers in the stowed state, so that nonzero-thickness panels of varying thicknesses may be accommodated in the folding pattern. Throughout this work, we assume a zero-thickness model, but note that the thickness-accommodating techniques of Tachi and/or Edmonson may be applied to any of the mechanisms described to realize a full thick-panel mechanism while preserving the single-DOF deployment motion.

2 Preliminaries

Figures 1 and 2 show implementations of the flasher structure by Scheel [12] and Palmer and Shafer [1] that illustrate the fundamental structure. There is a central planar region (henceforth, the *central polygon*) surrounded by a series of mountain and valley folds that emanate roughly radially, but are offset somewhat from being center-directed.

These images show curved and bent facets, but it is possible to create polyhedral (planar facet) versions of the flasher [3,8].

Manuscript received June 29, 2015; final manuscript received October 18, 2015; published online March 7, 2016. Assoc. Editor: Mary Frecker.

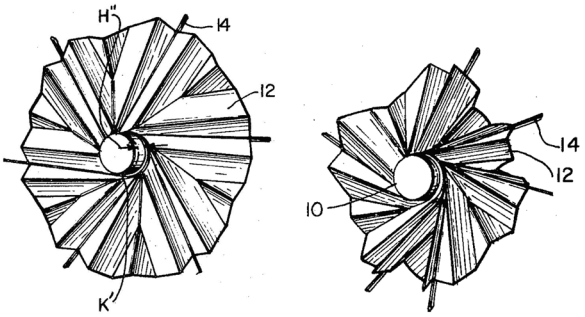

Fig. 1 Scheel's wind-up membrane. Left: nearly open. Right: starting to close. From Ref. [12].

Figure 3 shows three versions of a polyhedral flasher with a square central polygon and fourfold rotational symmetry constructed according to the algorithm of Ref. [8].

There are four distinct types of folds in a flasher, as illustrated in Fig. 4. The *diagonal folds* emanate from the corners of the central polygon and, in the folded form, propagate helically around the axis of symmetry. Next, there are *reverse* folds, which propagate axially around the structure, each fold forming a spiral that lies (nearly) in the same plane. Both reverse and diagonal folds are sharp folds, being folded nearly to $\pm\pi$. Next, there are the *bend* folds, which are (nearly) axis-parallel folds at the corners of the central polygon; they are the folds used for the layers to wrap around the central polygon. And last, there are the *central polygon* folds, which appear to be continuations of the reverse folds but, unlike the latter, have a fold angle of about $\pi/2$, rather than $\pm\pi$.

For a flasher to be rigidly foldable with a single DOF, the fold angles around each vertex must flex continuously in such a way that the fold angles along each fold are compatible when they meet up at every vertex. In general with flashers, this is not possible; for all of the patterns shown to date, at the very least, facets must bend along their diagonals. A general flasher pattern consists of degree-6, degree-5, and degree-4 vertices, with the last usually being the most numerous. Degree-4 vertices individually have a single DOF in their motion, and it will be these vertices that are the key to realizing single-DOF motion for a flasher. We now review briefly the important and relevant properties of degree-4 vertices.

3 Degree-4 Vertices

Figure 5 shows a generic degree-4 vertex, with four *sector angles* $\alpha_i, i = 1, \ldots, 4$, and four *dihedral angles*, $\gamma_i, i = 1, \ldots, 4$, with $\gamma_i \in [-\pi, \pi]$. For mountain folds, $\gamma_i < 0$; for valley folds, $\gamma_i > 0$. If $|\gamma_i| = \pi$, the fold is *fully folded*; if $|\gamma_i| \in (0, \pm\pi)$, it is *partially folded*; and if $\gamma_i = 0$ it is *unfolded*.

If all four creases are partially or fully folded, then there must be three mountains and one valley or three valleys and one mountain [13]. If we look at alternating (not consecutive) folds around the vertex, two will be of the same type and the other two will be of opposite type. We call the two folds of the same type (γ_2 and γ_4 in Fig. 5) the *major folds* (or major pair) of the vertex. The two folds of the opposite type (γ_1 and γ_3 in Fig. 5) are the *minor folds* of the vertex.

We also recognize two special cases: if $\alpha_1 + \alpha_4 = \alpha_2 + \alpha_3 = \pi$, the vertex is *straight-major*, because the major folds are collinear. Similarly, if $\alpha_1 + \alpha_2 = \alpha_3 + \alpha_4 = \pi$, the vertex is *straight-minor*.

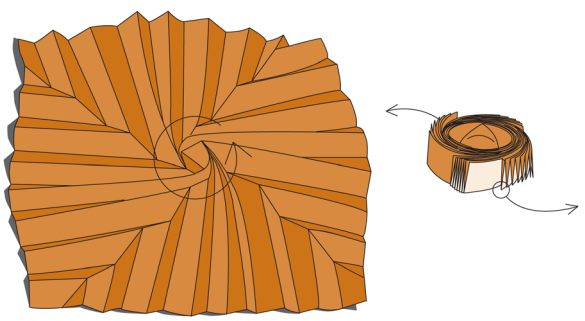

Fig. 2 The Palmer–Shafer origami flasher. Left: nearly fully deployed. Right: stowed. From Ref. [1].

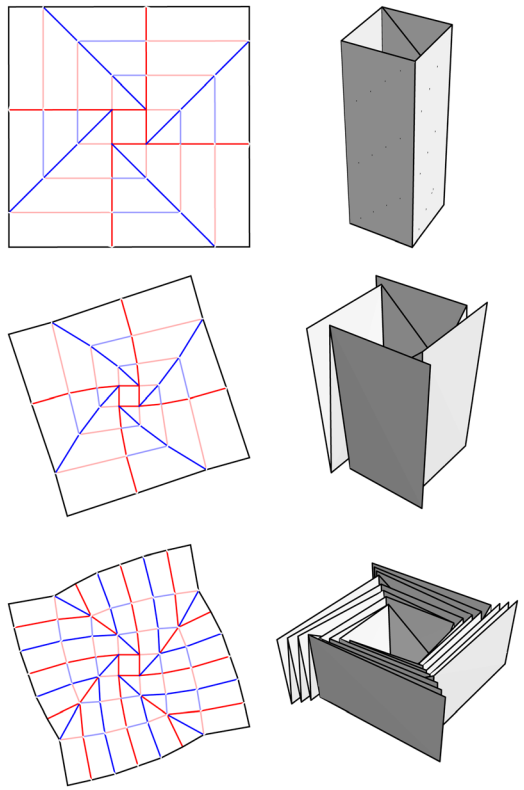

Fig. 3 A polyhedral flasher with fourfold rotational symmetry. Top row: an ideal polyhedral flasher (left: crease pattern and right: folded form). Middle row: the same structure, modified to spread the layers to accommodate nonzero thickness. Bottom row: the same structure, but with additional reverse folds added to reduce the height. Note that the crease patterns and folded forms are shown at different scales; the diameter of the folded form is approximately the diameter of the central polygon of the crease pattern in each case.

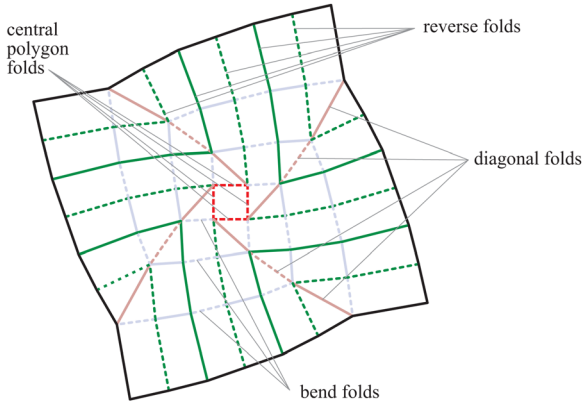

Fig. 4 The four distinct types of fold in a flasher. Here, we use the origami convention of drawing mountain folds as solid lines, valleys as dashed, with different tones for the four families of fold.

Straight-minor vertices are perfectly well behaved, but straight-major vertices are a special case; it is not possible for all four folds of a straight-major vertex to be partially folded at the same time. For a straight-major vertex to fold, first, γ_2 and γ_4 must fold from 0 to $\pm\pi$, and only then can γ_1 and γ_3 fold (and then only if $\alpha_1 = \alpha_4$ and $\alpha_2 = \alpha_3$).

For non-straight-major vertices, if one fold angle is chosen, the other three are fully determined from trigonometric relationships between the sector angles and the fold angles. For the generic case, these relationships can be rather complex (as shown in the Appendix). However, for a flat-foldable vertex—one that can be pressed flat with all layers in a common plane—the relations collapse to simple forms.

First, as is well known from Kawasaki's theorem [14], a degree-4 vertex is flat-foldable if and only if

$$\alpha_1 + \alpha_3 = \alpha_2 + \alpha_4 = \pi \tag{1}$$

For a flat-foldable vertex, the major fold angles are equal [15]

$$\gamma_2 = \gamma_4 \tag{2}$$

and the minor fold angles are equal and opposite [15]

$$\gamma_1 = -\gamma_3 \tag{3}$$

The relationship between adjacent fold angles has been described by several authors [13,15,16]; a particularly simple and useful expression (derived in the Appendix) is

$$\frac{\tan\frac{1}{2}\gamma_2}{\tan\frac{1}{2}\gamma_1} = -\frac{\tan\frac{1}{2}\gamma_2}{\tan\frac{1}{2}\gamma_3} = \frac{\tan\frac{1}{2}\gamma_4}{\tan\frac{1}{2}\gamma_1} = -\frac{\tan\frac{1}{2}\gamma_4}{\tan\frac{1}{2}\gamma_3} = \frac{\sin\frac{1}{2}(\alpha_1+\alpha_2)}{\sin\frac{1}{2}(\alpha_1-\alpha_2)} \tag{4}$$

Equation (4) also gives some justification for the names "major" and "minor"; a consequence of Eq. (4) is that

$$|\gamma_{2,4}| \geq |\gamma_{1,3}| \tag{5}$$

with strict inequality at all partially folded angles and equality only at the flat (fully unfolded and fully folded) states. So, away from the flat state, major folds are always larger than minor folds at a flat-foldable degree-4 vertex.

We define the ratio in Eq. (4) as the *fold angle multiplier* μ for the vertex. In general, $\mu > 1$. The fold angle multiplier is a measure of the *geometric advantage* between a major and minor fold of the vertex. If we denote either major fold angle by γ_+ and either minor fold angle by γ_-, we have that

$$\lim_{\gamma_-\to 0}\frac{d\gamma_+}{d\gamma_-} = \pm\mu,\ \lim_{\gamma_-\to\pi}\frac{d\gamma_+}{d\gamma_-} = \pm 1/\mu, \text{ and } \left|\frac{d\gamma_+}{d\gamma_-}\right| \in (1/\mu, \mu) \text{ at angles in between} \tag{6}$$

There is a remarkable property implicit in Eqs. (2)–(4), noted by Tachi [16]. For any two angles γ_i, γ_j at a flat-foldable degree-4 vertex, $\tan(1/2)\gamma_i / \tan(1/2)\gamma_j = \text{constant}$, independent of the state of foldedness. This property extends to any mesh of degree-4 vertices: if γ_i and γ_j are connected by a path containing only non-straight-major flat-foldable degree-4 vertices, their half-angle-tangents are proportion by some fixed value that depends on the sector angles around all of the vertices along the path. Because of this constant of proportionality, it is guaranteed that γ_i, γ_j, and all folds in between can fold smoothly all the way from flat to fully folded, at least, if we ignore all vertices outside the path. And, more broadly, for a mesh whose interior vertices are all flat-foldable degree-4 vertices, if we can find a partially folded state involving all folds for a single fold angle, then it is guaranteed that the entire pattern folds smoothly over the full range of fold angles from fully flat to fully folded, with a single DOF.

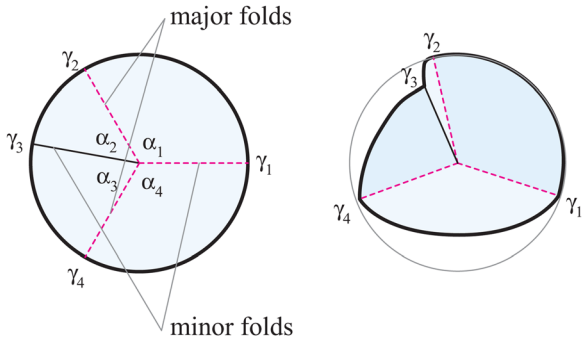

Fig. 5 A degree-4 vertex. Left: crease pattern. Right: folded form.

This property is extremely powerful and useful, and we can employ it when we are seeking single-DOF folding mechanisms. If we can construct a fold pattern consisting of flat-foldable degree-4 vertices and find a single consistent partially folded state, then we have a single-DOF mechanism. In principle, such a pattern could fold from flat unfolded to flat fully folded. In practice, self-intersection may limit the full range of motion, but even if we do not need full flat-foldability, we can still use this technique to achieve single-DOF mechanisms. And, we will now do this with flashers.

4 Simple Flashers

4.1 Fold Angle Relations. We now turn our attention back to the flasher. For simplicity, we will consider first a flasher that has no reverse folds at all, such as the one illustrated in Fig. 6. There are only diagonal, bend, and central polygon folds. This choice ensures that all of the interior vertices of the pattern are degree-4.

We will first look at the constraints on the angles in the pattern, assuming m-fold rotational symmetry on the positions of the fold lines, m-fold rotational symmetry on the magnitudes of the fold angles, and $m/2$-fold rotational symmetry on the sign of the fold angles (mountain/valley assignment). We also assume (at least initially) that m is even and $m \geq 4$. The central polygon is a regular m-gon, and so the interior angles at its corners are $(\pi - 2\pi/m)$. We take δ to be the angle between the incident diagonal fold and the side of the central polygon. In Fig. 6, we have $m = 4$ and the central polygon is a square.

Moving out along the diagonal folds, we have a sequence of degree-4 vertices. Denote the two angles to left and right of the

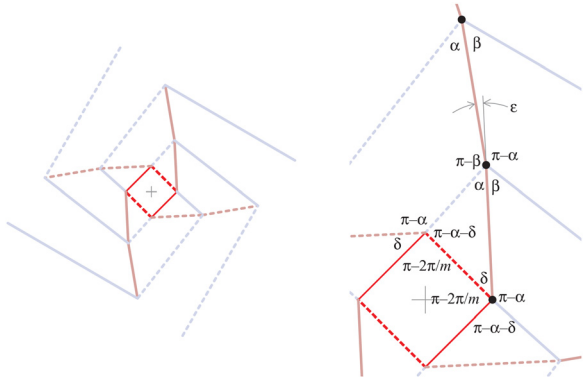

Fig. 6 A simplified flasher, containing only diagonal, bend, and central polygon folds. Left: the full crease pattern. Right: a close-up, with labeled sector angles.

diagonal fold as α and β, respectively. If we are going to attempt to create a single-DOF mechanism using the property described in Sec. 3, then this vertex must be flat-foldable, with opposite angles summing to π. This allows us complete the sector angle assignment around this vertex—and, as well, around all of the other degree-4 vertices. Since, according to Eqs. (2) and (3), the major and minor folds around each of the degree-4 vertices are equal, this means that the fold angles of all of the diagonal folds are equal to one another in magnitude, and the fold angles of all of the bend folds are equal to one another in magnitude. We denote the magnitude of the diagonal fold angles by γ_{diag} and the magnitude of the bend fold angles by γ_{bend}.

All of the degree-4 vertices are similar to one another (similar in the geometric sense), and because of that, the diagonal and bend fold angles at each degree-4 vertex are related to each other by Eq. (4). So, up to now, the sector angles and fold angles are consistent with one another at every degree-4 vertex. Since each degree-4 vertex is a single-DOF mechanism, the entire array of degree-4 vertices (apart from those of the central polygon) must be, itself, a single-DOF mechanism—if, that is, it is not locked by other interactions.

We have not yet considered the degree-4 vertices around the central polygon. If we force each central polygon vertex to be developable (its sector angles sum to 2π), so that the crease pattern is a flat sheet, that condition allows us solve for α

$$\alpha = \frac{\pi}{2} - \frac{\pi}{m} \tag{7}$$

While α is given by Eq. (7), angles β and δ may be chosen independently. But there is not complete freedom to choose. Looking at one of the vertices along the diagonal fold, if we choose $\beta = \alpha$, then the major folds at that vertex become collinear, resulting in the straight-major condition. As noted above, in a straight-major vertex, the major and minor folds become uncoupled; such a vertex must fold entirely from flat to fully folded along the major crease before the minor crease can fold at all (if even possible). So $\beta = \alpha$ is forbidden if we want a single-DOF mechanism where all the folds happen together.

It is convenient to introduce a new angle, ε, as the deviation from straightness of the major folds, as illustrated in Fig. 6. We then have

$$\beta = \alpha + \varepsilon \tag{8}$$

And because we now know the sector angles around these vertices, we can compute the fold angle multiplier between the major folds (diagonal folds) and minor folds (bend folds) at each vertex. We denote this fold angle multiplier by μ_{db}. It is given by

$$\mu_{db} = \cos\alpha + \cot\frac{\varepsilon}{2}\sin\alpha \tag{9}$$

If we choose any bend fold angle γ_{bend}, then every other bend fold has the fold angle $\pm\gamma_{\text{bend}}$, with the sign depending on its mountain/valley assignment, and every diagonal fold has the fold angle

$$\pm\gamma_{\text{diag}} = \pm 2\tan^{-1}\left(\mu_{\text{db}}\tan\frac{1}{2}\gamma_{\text{bend}}\right) \tag{10}$$

with, again, the sign determined from the mountain/valley assignment.

4.2 Consistency in the Middle. Now we consider fold angles around the central polygon, and here a problem arises. Consider the black-dotted central polygon vertex in Fig. 6. It is clearly not flat-foldable, because opposite angles sum to $(\pi/2 + \pi/m)$, not π. It is still a single-DOF mechanism, and so if we choose a generic value of the diagonal fold angle, γ_{diag}, we can compute the fold angles of the two incident central polygon folds (which will, in general, be different from one another in magnitude, as well as sign).

Let us denote the dihedral angle of the valley fold of the central polygon by $\gamma_{\text{cp},v}$ and that of the mountain fold by $\gamma_{\text{cp},m}$. Using the general expressions for opposite and adjacent dihedral angles from the Appendix and the angles from Fig. 6, we can solve for both $\gamma_{\text{cp},v}$ and $\gamma_{\text{cp},m}$ in terms of γ_{diag}. The expressions are both rather large, and we omit them for brevity, but the important thing is this: they are quite *different*.

The problem is that if we move to the next central polygon vertex and compute the fold angles for the two incident central polygon folds, we will get the same two values, but with opposite sign. Consistency from one vertex to the next therefore requires that

$$\gamma_{\text{cp},m} = -\gamma_{\text{cp},v} \tag{11}$$

and this is not the case; they have fundamentally different functional dependence upon γ_{diag}, no matter what values of α and δ might be chosen. So it is not possible to find an assignment of fold angles around the central polygon consistent with the single-DOF mechanism surrounding it.

Well, then: How about if we simply cut out the central polygon entirely, so that its edges now become edges of the fold pattern? Then, there would no longer be a consistency condition on the fold angles around each vertex of the central polygon because there are no central polygon fold angles to contend with.

But there is still a consistency condition to consider. In fact, it just got more complicated: by adding a hole, consistency must be satisfied in both rotation angle (3DOF) and translation (three more DOF). By design, all six conditions are satisfied at the unfolded and fully folded state. However, for a single-DOF mechanism, both must be satisfied across the full range of motion.

If we cut out the central polygon, at each of its vertices, we have three fixed sector angles and two fold angles whose values are linked by the single-DOF mechanism, and so we can solve for the angle between two adjacent sides of the central polygon—what would have been the interior angle of the central polygon.

We compute this angle by making use of 3D rotation matrices. Define the usual rotation matrices about the x, y, and z axes as

$$\begin{aligned}
\mathbf{R}_{\mathbf{x}}(\phi) &\equiv \begin{pmatrix} 1 & 0 & 0 \\ 0 & \cos\phi & -\sin\phi \\ 0 & \sin\phi & \cos\phi \end{pmatrix} \\
\mathbf{R}_{\mathbf{y}}(\phi) &\equiv \begin{pmatrix} \cos\phi & 0 & \sin\phi \\ 0 & 1 & 0 \\ -\sin\phi & 0 & \cos\phi \end{pmatrix} \\
\mathbf{R}_{\mathbf{z}}(\phi) &\equiv \begin{pmatrix} \cos\phi & -\sin\phi & 0 \\ \sin\phi & \cos\phi & 0 \\ 0 & 0 & 1 \end{pmatrix}
\end{aligned} \tag{12}$$

Left-multiplying a vector by matrix $\mathbf{R}_{\mathbf{x}}(\phi)$ rotates the vector through angle ϕ about the global x-axis, similarly for $\mathbf{R}_{\mathbf{y}}(\phi)$ and $\mathbf{R}_{\mathbf{z}}(\phi)$. If we have a local coordinate system defined by a 3×3 matrix, then we can rotate that coordinate system about its own local axes by *right-multiplying* by the transpose of these same matrices. We set up a coordinate system centered on the central polygon vertex whose local x-axis runs along $\gamma_{\text{cp},m}$ and whose local x–y plane contains folds $\gamma_{\text{cp},m}$ and γ_{bend} and describe this coordinate system by some matrix $\mathbf{I}$. Then, we can find the direction vector for fold $\gamma_{\text{cp},v}$ by successively rotating the coordinate system about the local z-axis for each sector angle and about the local x-axis for each dihedral angle as we work our way around the vertex. The transformed coordinate system is thus given by

$$\begin{aligned}
\mathbf{I}' = \mathbf{I}\cdot\mathbf{R}_{\mathbf{z}}^{\mathrm{T}}(\pi-\alpha-\delta)\cdot\mathbf{R}_{\mathbf{x}}^{\mathrm{T}}(\gamma_{\text{bend}}) \\
\mathbf{R}_{\mathbf{z}}^{\mathrm{T}}(\pi-\alpha)\cdot\mathbf{R}_{\mathbf{x}}^{\mathrm{T}}(\gamma_{\text{diag}})\cdot\mathbf{R}_{\mathbf{z}}^{\mathrm{T}}(\delta)
\end{aligned} \tag{13}$$

If the first component of $\mathbf{I}$ was the direction vector of fold $\gamma_{\text{cp},m}$, then the first component of $\mathbf{I}'$ should be the direction vector of

fold $\gamma_{cp,v}$, and their dot product must be the cosine of the angle between the twofold in 3D. We denote that angle by α_{3D}. Its angle cosine is

$$\begin{aligned}\cos\alpha_{3D} = \cos\alpha\Big(&\cos\delta\cos(\alpha+\delta) + \sin\delta\sin(\alpha+\delta)\cos\gamma_{bend}\cos\gamma_{diag}\Big)\\ &+\sin(\alpha+\delta)\big(\sin\delta\sin\gamma_{bend}\sin\gamma_{diag} - \sin\alpha\cos\delta\cos\gamma_{bend}\big)\\ &+\sin\alpha\sin\delta\cos(\alpha+\delta)\cos\gamma_{diag}\end{aligned} \tag{14}$$

Unfortunately, this quantity *varies* as the rest of the mechanism changes its folded state (i.e., as γ_{bend} and γ_{diag} vary, which they do together). In the flat, unfolded state, the edges of the central polygon form a closed polygon. But, it turns out, for nearly all other partially folded states, the corner angles change, and so the central polygon no longer closes up. That means we fail to satisfy translational consistency going around the central polygon.

Perhaps, a different choice of angles in the initial design would allow consistency, some magic combination? Unfortunately not, α_{3D} varies across the motion for every nonzero value of ε.

Perhaps, instead, we could remove more material around the center? Again, no. Consistency failure for a single loop around the center means that *any* loop that encloses the central polygon would fail in the same way (just with much greater algebraic complexity).

And so, there is no consistent assignment of sector and fold angles that makes this pattern an isometric mechanism. We are almost there: we can achieve consistency, isometry, and single-DOF motion at every other interior vertex, but the fold pattern fails when we require consistency going around the loop of the central polygon.

The solution, therefore, is to break the loop; we cut the pattern from the outside edge in to the center, so that there is no longer a loop condition around the central polygon to be satisfied. The cut path can be anywhere from the outside in, but for simplicity, we will cut along one of the diagonal folds, as illustrated in Fig. 7 and then remove the central polygon.

And that resolves the conflict! We now have a pattern consisting entirely of degree-4 vertices in which the fold angles and sector angles at each interior vertex are mutually consistent at every folded state, from unfolded to fully flat (or as close to fully flat as we can get without self-intersection).

We note that the idea of cutting a flasher from edge to center is not without precedent. Tibbalds et al. introduced the notion of cutting multiple panels of a disklike form apart in order to produce a single-DOF mechanism [17] at the cost of introducing multiple sets of struts. If we create a single-DOF flasher, though, then we only need to create a single cut, and we end up with a single connected single-DOF mechanism.

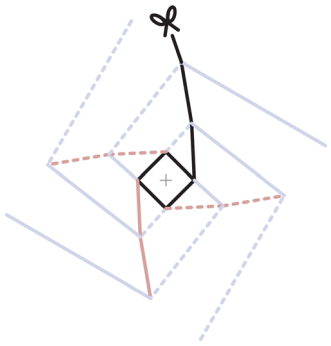

Fig. 7 Cut lines on the simple flasher. We cut out the central polygon and cut in from the edges along a diagonal fold.

4.3 Vertex Coordinates. So what does this pattern look like when folded? For that, we need to compute the vertex coordinates in 2D and 3D.

We denote each vertex of the crease pattern by $\mathbf{p}_{i,j}$, where $i = 0, \ldots$ indexes the vertices heading out along the diagonal folds from the central polygon, and $j = 0, \ldots, m$ denotes the rotational position around the origin, as illustrated in Fig. 8. Rotational indices "wrap around": $\mathbf{p}_{i,m} = \mathbf{p}_{i,0}$, and so forth.

We assume for simplicity that $\mathbf{p}_{0,0} = (1, 0)$.

Define the 2D rotational matrix

$$\mathbf{R}_m(k) \equiv \begin{pmatrix} \cos\dfrac{2\pi k}{m} & -\sin\dfrac{2\pi k}{m} \\ \sin\dfrac{2\pi k}{m} & \cos\dfrac{2\pi k}{m} \end{pmatrix} \tag{15}$$

Then, we have that

$$\mathbf{p}_{i,j} = \mathbf{R}_m(j) \cdot \mathbf{p}_{i,0} \tag{16}$$

We further define angles $\phi_{i,j}$ and $\theta_{i,j}$ as the absolute angles (measured in a global coordinate system as a rotation from the x-axis) of the fold lines emanating from $\mathbf{p}_{i,j}$, as illustrated in Fig. 8. From consideration of the angles in Fig. 6, we have that

$$\theta_{i,j} = (\pi - \delta - \alpha) + i\varepsilon + 2\pi j/m \tag{17}$$

$$\phi_{i,j} = (-\delta) + i\varepsilon + 2\pi j/m \tag{18}$$

Now, we can compute the position of $\mathbf{p}_{i,j}$ for $i > 0$ as the intersection of lines emanating from lower-i vertices. We introduce the vector-valued function

$$\mathbf{u}(\xi) \equiv (\cos\xi,\ \sin\xi) \tag{19}$$

the matrix determinant

$$\det(\mathbf{x}, \mathbf{y}) \equiv \begin{vmatrix} x_1 & y_1 \\ x_2 & y_2 \end{vmatrix} = x_1 y_2 - y_1 x_2 \tag{20}$$

and the line intersection function $\text{LINEINT}(\mathbf{a}_1, \mathbf{d}_1, \mathbf{a}_2, \mathbf{d}_2)$ that returns the intersection between two lines emanating from points $\mathbf{a}_1$ and $\mathbf{a}_2$ with direction vectors $\mathbf{d}_1$ and $\mathbf{d}_2$, given by

$$\text{LINEINT}(\mathbf{a}_1, \mathbf{d}_1, \mathbf{a}_2, \mathbf{d}_2) = \mathbf{a}_1 + \mathbf{d}_1 \frac{\det((\mathbf{a}_2 - \mathbf{a}_1), \mathbf{d}_2)}{\det(\mathbf{d}_1, \mathbf{d}_2)} \tag{21}$$

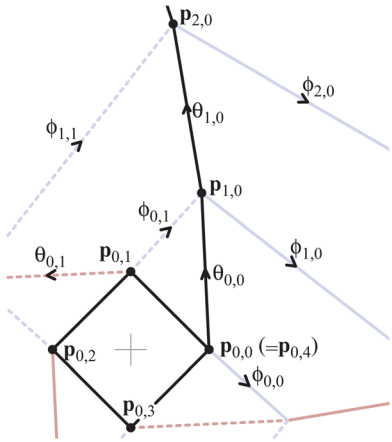

Fig. 8 Vertex and angle indexing in the simple flasher

Then,

$$\mathbf{p}_{i+1,0} = \text{LINEINT}\left(\mathbf{p}_{i,0}, \mathbf{u}(\theta_{i,0}), \mathbf{p}_{i,1}, \mathbf{u}(\phi_{i,1})\right) \tag{22}$$

This relation, plus Eq. (16), allows us to recursively compute all of the points of the crease pattern, for as far out as we wish to go.

An open question is what to do for the outer boundary of the pattern. For simplicity, we have chosen to simply close the pattern by connecting the points $\mathbf{p}_{n,j}$ for some value n.

What about the folded form? Since we know the crease pattern, and we know the angle of all of the folds, we can compute the folded form by rotating the facets of the crease pattern relative to their neighbors about the known fold angles of their shared creases. This is done efficiently by constructing a spanning tree on the facets linked by their adjacency, then traversing the tree and composing rotations along the way.

Using these formulas, we have computed representative examples of single-DOF flasher mechanisms. An example is shown in Fig. 9 for parameters $m = 4$, $n = 3$, $\varepsilon = 3$ deg, $\delta = 43.5$ deg, and γ_{bend} taking on various values from 0 (fully flat) to (nearly) fully folded.

The 3D plots verify the impossibility of achieving a closed central polygon. As can be seen in the first few images, the central polygon opens up quite widely, then (in the middle image) it begins to curl up on itself. The maximum value of γ_{bend} in the figure was chosen to be the point at which the central polygon closes back up on itself—and, not incidentally, the originally cut edges of the ring meet up with each other once more.

It is possible to take the pattern all the way to a bend fold angle of $\gamma_{\text{bend}} = 180$ deg, i.e., fully flatly folded, at which point the entire pattern lies in a common plane. However, to get there, the panels of the pattern must intersect each other in numerous places and ways. No practical application would take this structure all the way to flatly folded (at least none that we can envision at present). The stowed state for this structure stops when the central polygon recloses and the panels have some small dihedral angle between them. Such a model may be used in a thickening algorithm, such as that of Tachi [9], which requires slightly angularly separated panels.

There are two noticeably different motions in going from the flat to the curled-up state. First, for small γ_{bend}, most of the motion happens on the diagonal folds, and as they fold up, the flat disk forms into a slightly curved vertical stack of layers. There then comes a point where the diagonal folds are mostly folded, and the remaining motion comes from the bend folds curling the layers around until they meet up again.

4.4 The Central Region. In general, the vertices of the central polygon are nonplanar in the partially folded state. However, we have found that a particular value of δ gives rise to a central polygon that is planar through the full range of motion:

$$\delta_{\text{planar}} = \frac{\pi}{m} - \frac{\varepsilon}{2} \tag{23}$$

We chose $\delta = \delta_{\text{planar}}$ in Fig. 9.

As noted already, as the mechanism proceeds away from the flattened state, the central polygon opens up, and then it recloses. The "fully stowed" state would be that where the central polygon has closed to its original state and the edges of the cut have come back together. We would like to know what bend angle γ_{bend} gives rise to this state: this would define the full range of useful motion of the mechanism.

Recall that Eq. (14) gave the cosine of the angle between folds $\gamma_{\text{cp},m}$ and $\gamma_{\text{cp},v}$, which was $\alpha_{3\text{D}}$. The mechanism has reclosed when that angle takes on the value of the interior angle of the original planar central polygon, whose angle cosine is

$$\cos\alpha_0 = \cos\left(\pi - \frac{2\pi}{m}\right) = -\cos\left(\frac{2\pi}{m}\right) \tag{24}$$

So we can equate $\cos\alpha_{3\text{D}}$ from Eq. (14) and $\cos\alpha_0$ from Eq. (24) and solve for the bend angle (or equivalently, the diagonal angle) that satisfies the equality.

To keep the algebra tractable, we introduce the Weirstrauss substitution

$$x \equiv \tan\frac{\gamma_{\text{bend}}}{2} \tag{25}$$

which gives rise to the following simplifying substitutions:

$$\begin{aligned}
\sin\gamma_{\text{bend}} &= \frac{2x}{1+x^2} \\
\cos\gamma_{\text{bend}} &= \frac{1-x^2}{1+x^2} \\
\sin\gamma_{\text{diag}} &= \frac{2(\mu_{db}x)}{1+(\mu_{db}x)^2} \\
\cos\gamma_{\text{diag}} &= \frac{1-(\mu_{db}x)^2}{1+(\mu_{db}x)^2}
\end{aligned} \tag{26}$$

Substituting these into Eq. (14) along with taking $\delta = \delta_{\text{planar}} = \pi/m - \varepsilon/2$, $\mu_{db} = \cos\alpha + \cot\varepsilon/2\sin\alpha$, and $\alpha = \pi/2 - \pi/m$ gives

$$\begin{aligned}
\cos\alpha_{3\text{D}} = &\left(x^2\left[(x^2+1)\sin\left(\frac{2\pi}{m}\right)\sin(\varepsilon) + x^2 - \cos(\varepsilon)\right]\right. \\
&\left. + \cos\left(\frac{2\pi}{m}\right)\left[-2x^2 + (x^4+x^2+1)\cos(\varepsilon) - 1\right]\right) \Big/ \\
&\left((x^2+1)\left[x^2\cos\left(\frac{2\pi}{m} - \varepsilon\right) + x^2 - \cos(\varepsilon) + 1\right]\right)
\end{aligned} \tag{27}$$

This angle cosine is parameterized on the variable x, which is the transformed version of γ_{bend}. We would like to know the value of x (and thus, by extension, γ_{bend}) that makes this value equal

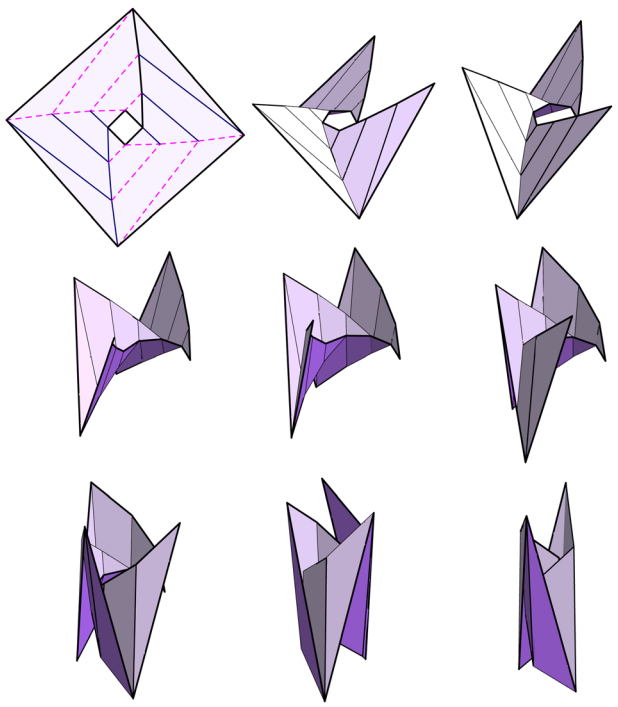

Fig. 9 A single-DOF flasher for various values of γ_{bend}. From upper left to lower right: $\gamma_{\text{bend}} = 0$ deg, 3 deg, 5 deg, 10 deg, 20 deg, 30 deg, 40 deg, 65 deg, and 87 deg. Note that the scale varies from one subfigure to the next.

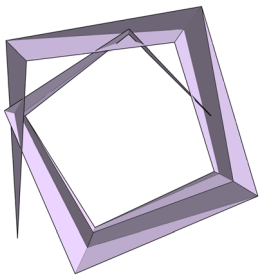

Fig. 10 A view from the top of the flasher of Fig. 9 for $\gamma_{\text{bend}} = 80$ deg, showing collisions with the inner layers

that of the planar central polygon. Setting the two values equal and solving for x gives two solutions: first, $x = 0$, which is the unfolded state. The second solution is the desired fully folded state. We find

$$x = \frac{\sec\left(\frac{\pi}{m}\right)}{\mu_{db}\sqrt{2}} \times \left[\mu_{db}^2\left(\cos\varepsilon - \cos\frac{2\pi}{m}\right) - 4\mu_{db}\cos\frac{\varepsilon}{2}\sin\left(\frac{\pi}{m} - \frac{\varepsilon}{2}\right) + \cos\left(\frac{2\pi}{m} - \varepsilon\right) - \cos\frac{2\pi}{m}\right]^{1/2} \tag{28}$$

which sets the maximum bend angle to be

$$\gamma_{\text{bend,max}} = 2\tan^{-1}\left[\sec\left(\frac{\pi}{m} - \frac{\varepsilon}{2}\right)\sqrt{\sin\left(\frac{\pi}{m}\right)\sin\left(\frac{\pi}{m} - \varepsilon\right)}\right] \approx \frac{2\pi}{m} - \varepsilon - \frac{1}{4}\cot\left(\frac{\pi}{m}\right)\varepsilon^2 + O(\varepsilon^3) \tag{29}$$

As we fold the pattern beyond $\gamma_{\text{bend,max}}$, the pattern self-intersects. There is also a small amount of self-intersection even before closure. This can be seen in Fig. 10, which is a view "looking down the barrel" of the tubular form just before the central polygon closes.

So, this is potentially a problem with practical applications of this structure. However, this collision happens because of where we chose our cut, which results in one portion of the pattern wrapping around another as we approach the stowed state. In the stowed state, the cut edges realign with one another. We can therefore begin with the curled-up state and make our cut somewhere else in a way that prevents this wrap-around issue. Two possible alternate locations for a cut are illustrated in Fig. 11.

Judicious choice of cut line can potentially eliminate self-intersection throughout the full range of motion, from stowed to fully deployed. We will show one such choice and its effects in Sec. 6.

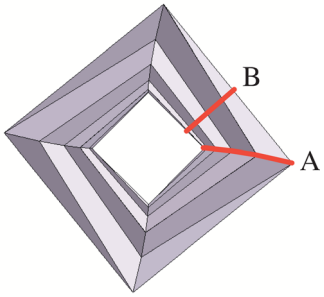

Fig. 11 A top view of the flasher with $m = 4$, $n = 3$, $\epsilon = 3$ deg, $\delta = 43.5$ deg, and $\gamma_{\text{bend}} = 87$ deg. Lines *A* and *B* indicate possible alternate cut lines.

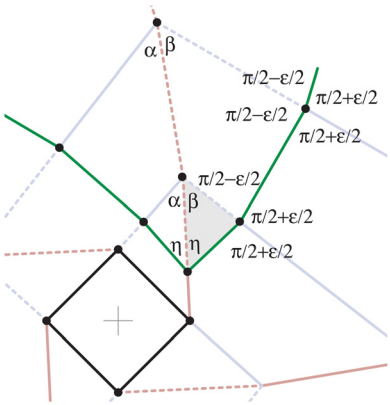

Fig. 12 Crease pattern with the addition of a pair of reverse folds along one of the diagonals

Another issue getting in the way of practical application is the fact that the stowed form is long and tubular, which arises from the fact that this is the simplest possible flasher structure. That length can be reduced by choosing a larger rotational order, but that strategy gives small slivers of triangles near the inner rim, which are undesirable in applications.

Scheel [12] and subsequent investigators show that one can reduce the height of a flasher by incorporating what in the origami world are called *reverse folds* into the pattern; such were included in the constructive algorithms of Guest and Pellegrino [3] and Zirbel et al. [8]. We can incorporate such folds into this flasher while preserving the single-DOF motion, as we show now.

5 Reduced-Height Flashers

We now consider adding a pair of reverse folds that emanates from some point along one of the diagonal folds, as illustrated in Fig. 12. We denote by η the angle that the reverse fold makes relative to the diagonal fold. In order to avoid disturbing the single-DOF mechanism that already exists, we will assume that the diagonal and bend folds are unchanged, except for the addition of vertices and selective inversion of the fold type (sign change of the fold angle). The name "reverse fold" comes from the origami world; such a set of folds inverts the parity of all of the diagonal and bend folds that lie within the V of the reverse fold.

What freedom do we have in the choice of η? If we are to leave the magnitude of the fold angles unchanged along the diagonal and bend folds, then all of the new vertices must be flat-foldable. That means that both sides of the base of the V (where the reverse folds hit the diagonal) must make the same angle η with the diagonal fold, as shown in Fig. 12.

It also means that each of the vertices where a reverse fold meets a bend fold must be geometrically similar to one another, as well as flat-foldable. Considering what happens at two successive vertices along a reverse fold reveals that there is only one possible set of sector angles at those vertices that make them all geometrically similar, namely, sector angles of $(\pi/2 - \varepsilon/2)$ and $(\pi/2 + \varepsilon/2)$ (two of each), as illustrated in Fig. 12.

With the four sector angles at each reverse/bend vertex assigned, the value of η is fully defined and can be worked out from the interior angles of the shaded triangle in Fig. 12. We find that

$$\eta = \frac{\pi}{2} - \alpha - \frac{\varepsilon}{2} = \frac{\pi}{m} - \frac{\varepsilon}{2} = \delta_{\text{planar}} \tag{30}$$

This is a nice result; it tells us that if we choose $\delta = \delta_{\text{planar}}$ and place the tip of the reverse fold V along the first diagonal fold, the left side of the V will be parallel to the edge of the central

polygon. If we place the tip of the reverse fold V on a vertex of the central polygon, then the left side will be coincident with the edge of the central polygon.

There is one thing still to check, however. We have three types of folds with distinct fold angle magnitudes: diagonal (γ_{diag}), bend (γ_{bend}), and now reverse (γ_{rvrs}). We also have three types of interior vertices that enforce proportionality between the half-angle-tangents of the fold angles at each vertex. Each vertex can be labeled by the two types of fold incident on the vertex: diagonal/bend (which we have already met, characterized by fold angle multiplier μ_{db}), and now two new ones: reverse/bend, which will be characterized by a fold angle multiplier μ_{rb}, and reverse/diagonal, with a fold angle multiplier μ_{rd}.

The shaded triangle in Fig. 12 has one of each type of vertex. There is a self-consistency condition that must be satisfied going around this triangle. In particular, we must have

$$\mu_{rb} = \mu_{rd}\mu_{db} \tag{31}$$

For a general triangle of three flat-foldable vertices, this relationship is not guaranteed to hold. What about this particular case?

The value of μ_{db} was given by Eq. (9). For the other two, we find that

$$\mu_{rb} = \csc\frac{\varepsilon}{2} \tag{32}$$

$$\mu_{rd} = \csc\left(\alpha + \frac{\varepsilon}{2}\right) \tag{33}$$

Substituting these into Eq. (31) reveals that the latter is satisfied for all values of α and ε. So, no matter what simple flasher we start with, we can add one or more reverse folds anywhere along the diagonal folds, and the resulting pattern is guaranteed to be a single-DOF mechanism.

Equation (29) gave the value of γ_{bend} at the maximally folded (stowed) state, $\gamma_{\text{bend,max}}$. We can substitute that value back into Eq. (10), to find γ_{diag} at the maximally folded state

$$\gamma_{\text{diag,max}} = 2\tan^{-1}\left[\csc\left(\frac{\varepsilon}{2}\right)\sqrt{\sin\left(\frac{\pi}{m}\right)\sin\left(\frac{\pi}{m}-\varepsilon\right)}\right] \tag{34}$$

And in the same vein, the reverse fold angle, γ_{rvrs}, at the maximally folded state will be

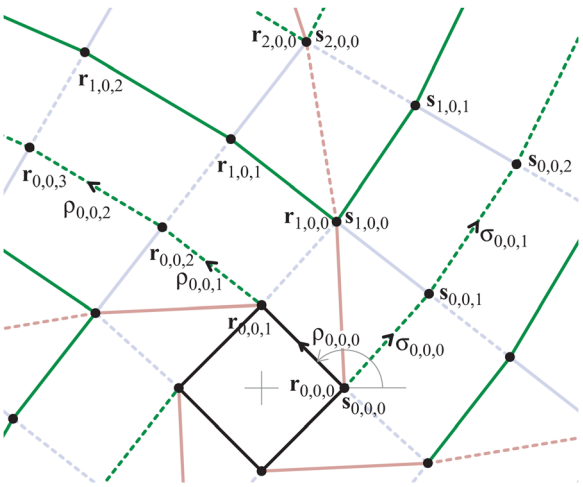

Fig. 13 A portion of the crease pattern of a reverse-folded flasher, with reverse folds emanating from each of the diagonal vertices

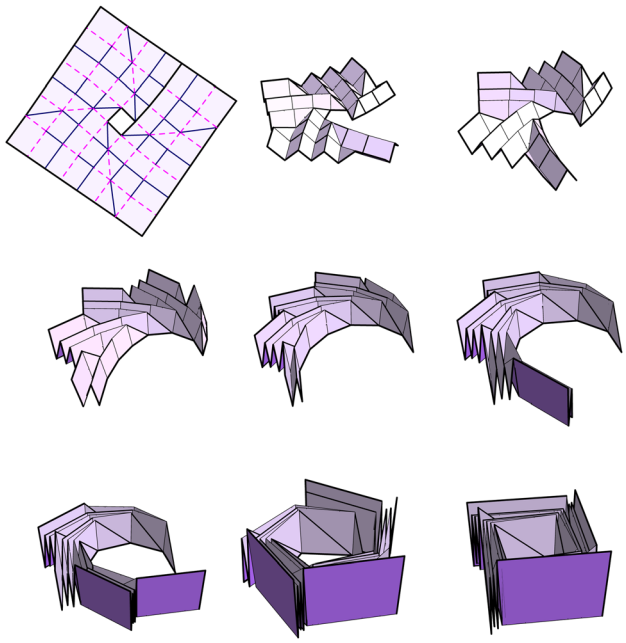

Fig. 14 A single-DOF reverse-folded flasher for various values of γ_{bend}. From upper left to lower right: $\gamma_{\text{bend}} = 0$ deg, 3 deg, 5 deg, 10 deg, 20 deg, 30 deg, 40 deg, 65 deg, and 87 deg.

$$\gamma_{\text{rvrs,max}} = 2\tan^{-1}\left[\csc\left(\frac{\varepsilon}{2}\right)\sec\left(\frac{\pi}{m}-\frac{\varepsilon}{2}\right)\times\sqrt{\sin\left(\frac{\pi}{m}\right)\sin\left(\frac{\pi}{m}-\varepsilon\right)}\right] \tag{35}$$

The spacing between successive reverse folds can be chosen arbitrarily. The farther apart successive reverse folds are placed, the taller the resulting mechanism.

When placing the reverse folds, one can think of each reverse fold as "sliding" along the diagonal, creating triangular and quadrilateral panels along each diagonal; each reverse fold breaks a diagonal fold into two segments whose lengths depend upon the position of the tip of the V of the reverse fold. There is a special case, where the tip of the V of the reverse fold coincides with an existing vertex along the diagonal. This choice gives rise to a particularly elegant crease pattern consisting of triangular facets along the diagonals and near-rectangular panels everywhere else.

It also creates degree-6 vertices along the diagonal, each created by the effective merging of two degree-4 vertices. This merging potentially increases the number of DOF of the mechanism—an issue we will come back to presently—but it does not alter the consistency between the values of γ_{bend}, γ_{diag}, and γ_{rvrs} given above.

We now compute 2D and 3D representations of this structure. We introduce triply subscripted points for the vertices of the reverse folds, as illustrated in Fig. 13.

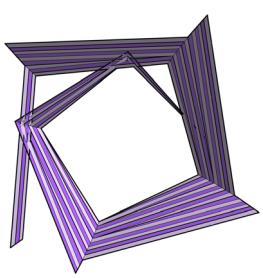

Fig. 15 A view from the top of the flasher of Fig. 14 for $\gamma_{\text{bend}} = 80$ deg, showing collisions with the inner layers

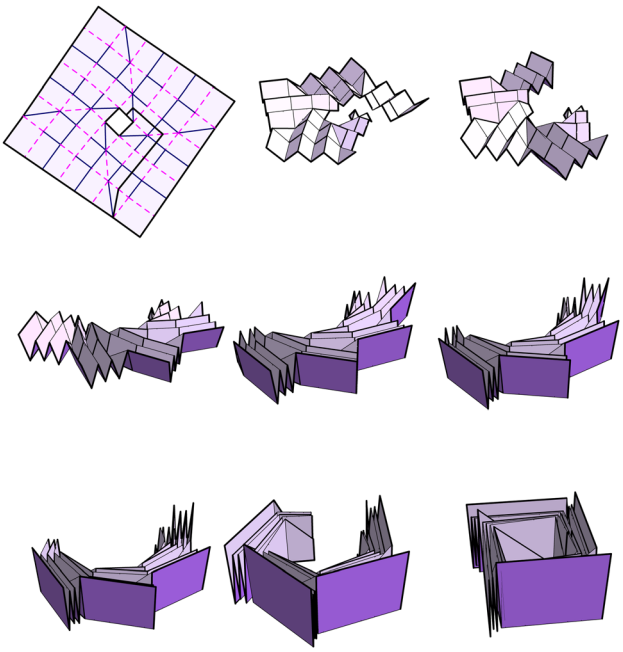

Fig. 16 A rigidly foldable flasher for various values of γ_{bend}. From upper left to lower right: $\gamma_{\text{bend}} = 0$ deg, 3 deg, 5 deg, 10 deg, 20 deg, 30 deg, 40 deg, 65 deg, and 87 deg.

In each rotational section, we define $\mathbf{r}_{i,j,k}$ for vertices on the left side of the diagonal fold and $\mathbf{s}_{i,j,k}$ for vertices on the right side (as viewed from the central polygon). For vertices on the diagonal folds, we define both

$$\mathbf{r}_{i,j,0} = \mathbf{s}_{i,j,0} \equiv \mathbf{p}_{i,j} \tag{36}$$

where $\{\mathbf{p}_{i,j}\}$ are the original vertices of the pattern as defined in Sec. 4. As we move out from $\mathbf{r}_{i,j,0}$ along a reverse fold, the k index of $\mathbf{r}_{i,j,k}$ increments each time we hit a bend fold, and similarly with $\mathbf{s}_{i,j,k}$.

We note that this gives multiple names to the same point; not only does $\mathbf{r}_{i,j,0} = \mathbf{s}_{i,j,0}$ but also $\mathbf{r}_{i,j,1} = \mathbf{r}_{i,j-1,0}$ and $\mathbf{s}_{0,j,k} = \mathbf{r}_{0,j-1,k+1}$. This requires a bit of care in the bookkeeping of distinct vertices, but otherwise causes no problems.

We further define $\rho_{i,j,k}$ as the absolute angle of the reverse fold emanating outward from $\mathbf{r}_{i,j,k}$, and $\sigma_{i,j,k}$ as the absolute angle of the reverse fold emanating outward from $\mathbf{s}_{i,j,k}$ (like $\theta_{i,j}$ and $\phi_{i,j}$, measured as a rotation relative to the x-axis in a global coordinate system).

With these definitions, the vertex coordinates and angles are as follows:

$$\rho_{i,j,k} = \theta_{i,j} + \eta + k\varepsilon \tag{37}$$

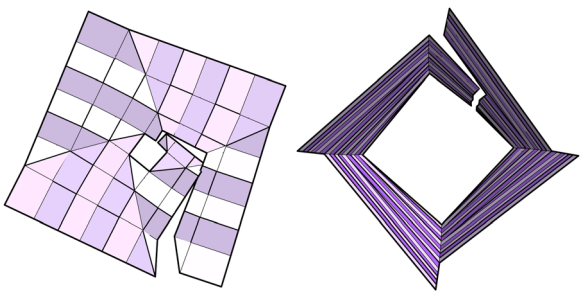

Fig. 17 A rigidly foldable flasher near the endpoints of the motion. Left: $\gamma_{\text{bend}} = 1$ deg. Right: $\gamma_{\text{bend}} = 85$ deg (different scale).

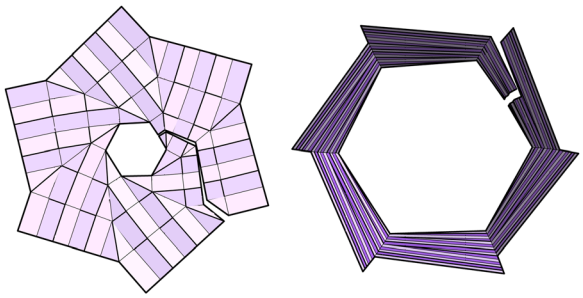

Fig. 18 A rigidly foldable hexagonal flasher near the endpoints of the motion. Left: $\gamma_{\text{bend}} = 0.5$ deg. Right: $\gamma_{\text{bend}} = 56$ deg (different scale).

$$\sigma_{i,j,k} = \theta_{i,j} - \eta + k\varepsilon \tag{38}$$

$$\mathbf{r}_{i,j,k+1} = \text{LINEINT}\left(\mathbf{r}_{i,j,k}, \mathbf{u}(\rho_{i,j,k}), \mathbf{p}_{i+k,j+1}, \mathbf{u}(\phi_{i+k,j+1})\right) \tag{39}$$

$$\mathbf{s}_{i,j,k+1} = \text{LINEINT}\left(\mathbf{s}_{i,j,k}, \mathbf{u}(\sigma_{i,j,k}), \mathbf{p}_{i+k+1,j}, \mathbf{u}(\phi_{i+k+1,j})\right) \tag{40}$$

where $\theta_{i,j}$ and $\phi_{i,j}$ were given by Eq. (17).

The outermost vertices are a special case, and their position depends on how we choose to finish the pattern. For the tubular flasher, we simply connected points $\{p_{n,j}\}$ for some n. Doing that with this reverse-folded case will slice some of the outermost panels, giving trapezoidal and/or triangular facets. For simplicity and elegance, we have chosen to terminate the pattern along what would be bend folds, which gives roughly rectangular panels for all panels not along the diagonal folds. We have also chosen the cut line along one of the reverse folds (specifically, along the $\mathbf{s}_{0,0,k}$ chain of folds), rather than along a diagonal, as in the previous example.

Figure 14 shows this new flasher design from unfolded to fully folded for the same parameters as Fig. 9, with $m = 4$, $n = 3$, and $\varepsilon = 3$ deg. Once again, we have a rigidly foldable single-DOF mechanism.

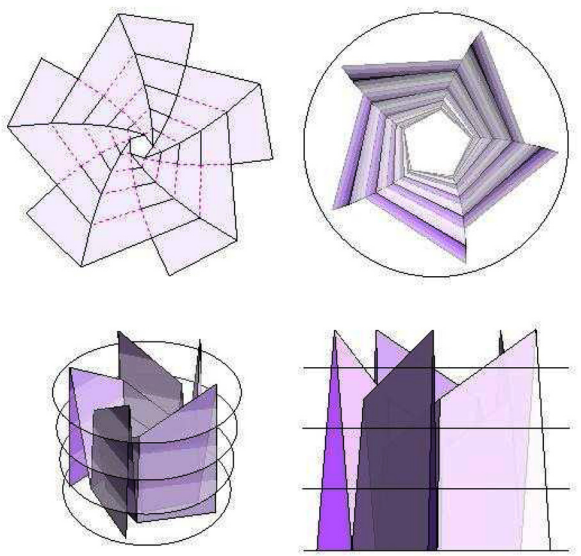

Fig. 19 A flasher with reverse folds only along the $\{\mathbf{s}_{0,j,k}\}$ and $\{\mathbf{r}_{0,j,k}\}$ lines with fivefold rotational symmetry. Top left: crease pattern. Top right: top view of the folded form. Bottom left: perspective view of the flasher with equally spaced cut planes. Bottom right: side view of same.

6 Layer Collision Avoidance

There is still the question of layer collisions. For the simulation of Fig. 14, we have cut the crease pattern along a reverse fold, rather than along a diagonal fold as in the simpler flasher. This cut still gives a layer collision as we approach the folded state, as can be seen in Fig. 15.

The presence of layer collisions depends upon the position and orientation of the cut. A straight cut in the flat state—either along a diagonal fold, as in the simple flasher, or along a reverse fold, as in the previous example—assumes a spiral form in the 3D state, and it is the overlap of that spiral that gives rise to the collision in the nearly stowed state. We can avoid such a collision by choosing a cut that is nearly straight in the stowed state, as was noted earlier in Fig. 11. Such a cut will give rise to a spiral cut in the flat state, but with appropriate choice of cut, can give rise to a collision-free motion as the fold angle approaches $\gamma_{\text{bend,max}}$.

In Fig. 16, we show a different cut position with otherwise the same parameters as Fig. 14. As before, this pattern moves rigidly between the deployed (flat) and stowed (cylindrical) shape.

By making the cut follow along a bend, we get the cut edges to more cleanly line up in the stowed state. As $\gamma \to \gamma_{\text{bend,max}}$, the cut edges realign and form a perfect butt joint.

However, this particular introduces a very slight layer intersection near the deployed state. Figure 17 shows top views in the nearly deployed and nearly stowed states.

This collision is slight and only results in a slight overlap; complete elimination of the intersection could be achieved with a slight removal of material from a few of the panels.

Contributing factors to the presence of collisions in the near-stowed state are the sharp corners in the bend that arises from low rotational order. In higher-rotational order, the residual overlap is reduced. Figure 18 shows a hexagonal flasher with the same cut pattern; in this pattern, there is still a very slight overlap in the near-stowed state, but it is extremely small, and only a tiny amount of material would need to be removed to eliminate the overlap.

It seems likely that an appropriately chosen path for the cut could entirely eliminate layer collisions; we leave that exploration as a topic for future work.

7 Constant-Height Flashers

The choice of initiating the reverse folds at existing vertices has a certain elegance and cleanliness to it, and it makes all panels either quadrilaterals or triangles. This choice has an important side effect: it creates several degree-6 vertices. The number of DOF of a degree-n vertex is $n-3$, so a degree-6 vertex has three, not one, DOF. This could, in principle, give the mechanism extra DOF.

However, those degree-6 vertices do not exist in isolation. The facets surrounding each degree-6 vertex are themselves connected to degree-4 vertices, and those vertices are constrained to single-DOF paths in phase space. If enough facets surrounding a high-degree vertex are constrained to single-DOF paths, then the remaining facets will also be clamped to the single-DOF motion, which happens in this mechanism.

Another potential drawback of locating reverse fold tips at existing bend vertices along the diagonal is that it gives each spiral ring a slightly different height, with inner rings being shorter than outer ones. (This behavior is most clearly visible in the last subfigure of Fig. 14.) This results in a less than optimal packing in the stowed state, since the space above the shorter rings is essentially wasted. It would be most efficient if each panel fully filled the vertical slice of space allocated to it by its vertical projection.

As we have already noted, the tip of any given V of reverse folds may be positioned anywhere along the diagonal fold while maintaining the kinematics of the mechanism, and if no reverse fold tips coincide with other vertices along the diagonal, then all of the vertices will be of degree-4 and all interior vertices and their incident facets will collectively exhibit single-DOF motion.

The freedom to place reverse folds anywhere along the diagonals allows us to make all of the spiral rings have exactly the same height in the stowed state, and that height can be independently selected as a design variable in the construction of the crease pattern.

We constructed both of the flashers presented thus far by selecting angles that enforce single-DOF rigid foldability at all degree-4 vertices. It turns out that this choice results in a fortuitous behavior: the vertices of each near-linear chain of reverse folds lie in a common plane throughout the full range of motion, and since the central polygon itself is planar for $\eta = \delta_{\text{planar}} = \pi/m - \varepsilon/2$, that means that many groups of vertices lie in a common plane throughout the full range of motion. In particular, the sets of vertices $\{\mathbf{s}_{0,j,k}\}$ and $\{\mathbf{r}_{0,j,k}\}$ all lie in the same plane as the central polygon throughout the full range of motion.

If we construct a flasher with those as the only reverse folds, we obtain a structure like that shown in Fig. 19, in which the bottom of the flasher lies in a horizontal plane, and each of the near-vertical facets makes the same angle with that plane, an angle of $\gamma_{\text{bend}}/2$. We could then envision cutting this conical structure in the stowed state with a series of horizontal planes spaced evenly in z; the intersection of each plane with the basic flasher thereby defines a set of reverse folds in the crease pattern, and the folded form that incorporates those reverse folds would be the result of

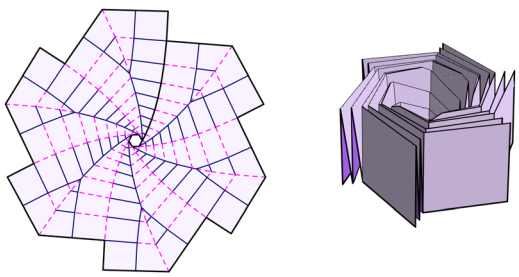

Fig. 20 A constant-height flasher for $m = 6$, $n_r = 9$, $\varepsilon = 3$ deg, and $h = 4.8$. Left: crease pattern. Right: folded form. In this flasher, the cut runs along the $\{s_{0,0,k}\}$ chain of creases.

Fig. 21 A wood veneer laminate fabricated constant-height flasher for $m = 6$, $n_r = 9$, $\varepsilon = 3$ deg, and $h = 4.8$. Top left: stowed state, top view. Top right: stowed state, side view. Bottom left: partially folded. Bottom right: deployed.

successive reflections of the folded form in the stack of planes, as illustrated in Fig. 19.

Suppose we start at point $\mathbf{p}_{0,0} = (1, 0)$ and travel outward along the diagonal fold a distance d, where d is measured along the chain of diagonal folds (making bends at each of the points $\{\mathbf{p}_{i,0}\}$). Then in the fully folded (stowed) form, i.e., when $\gamma_{\text{bend}} = \gamma_{\text{bend,max}}$, the height z of the point at distance d is given by

$$z(d) = d \sec\left(\frac{\varepsilon}{2}\right)\sqrt{\sin\left(\frac{\pi}{m}\right)\sin\left(\frac{\pi}{m} - \varepsilon\right)} \tag{41}$$

This can be turned around to determine the positions of the points of the V of each reverse fold as a function of the desired target height of the flasher. If h is the desired height, then each successive reverse fold along the jth diagonal should be initiated at a distance

$$d_k = h \cos\left(\frac{\varepsilon}{2}\right)\sqrt{\csc\left(\frac{\pi}{m}\right)\csc\left(\frac{\pi}{m} - \varepsilon\right)} \tag{42}$$

from the point $\mathbf{p}_{0,j}$ for $k = 1, \ldots, n_k$, with the reverse folds and vertices constructed along the diagonals and bend folds in the same way we constructed points $\{\mathbf{s}_{0,j,k}\}$ and $\{\mathbf{r}_{0,j,k}\}$. Now, the number of vertical divisions n_k is decoupled from the number of panels n_r in a single spiral. An example of such a constant-height flasher with hexagonal rotational symmetry is shown in Fig. 20.

Choosing a constant height for all the spiral reverse folds gives the most efficient possible stowed form by making full use of the vertical "airspace" above or below each tilted panel. In addition, displacing the reverse folds from the existing vertices along the diagonals, as in Fig. 20, ensures that all of the interior vertices are degree-4 vertices, making it easier to obtain a single-DOF mechanism even after adding a radial cut.

8 Example Fabrication

To verify the analysis presented above, we have fabricated several small test pieces, using laser-scored wood veneer laminate for ease of fabrication. The laminate used was Sanfoot wall covering, manufactured by Hokusan Corporation, which consists of a polymer-infused wood veneer sandwiched with layers of foil and polymer, with a total thickness of 0.34 mm. We then laser-scored creases by scoring through the upper wood polymer layers, using the foil layer as a blocking layer to prevent cutting through the lower polymer layers, thereby creating flexible polymer hinges from the layers below the foil. The wood and polymer laminate creates stiff, nonstretchable/nonwrinklable facets. The scored lines create flexible hinges with little excess play in the hinges owing to the narrow width of the laser cuts (~0.1 mm), and the overall thinness of the material means that we can get close to zero-thickness theoretical behavior without having to implement more complex thickness-compensating fabricational techniques (e.g., Refs. [9] and [10]).

We typically laser-scored complete (uncut) flasher patterns, then manually introduced the radial cut by cutting the pattern with a sharp knife. This allowed us to quickly examine the effects of different radial cut patterns without having to build them programmatically into the parameterized model that generated the crease pattern.

Figure 21 shows photographs of one such flasher, using the pattern from Fig. 20, in the flat (deployed), partially folded, and fully stowed states.

Manual manipulation of these test models verifies the single-DOF motion of the theoretical behavior, which is the case for arbitrarily stiff panels and arbitrarily free hinges. Real materials, of course, are not perfectly stiff and/or free, and in the thin wood veneer models, some residual flexing of panels gives rise to some additional bending modes, in much the same way that a single-DOF Miura-ori possesses twisting modes that rely on flexing of the panels.

With suitable choice of fabrication technologies, such parasitic modes can undoubtedly be minimized. However, there is an inherent problem in mechanisms based on flat-foldable degree-4 vertices such as this one (and the venerable Miura-ori [11], among others). In general, the greatest stacking efficiencies arise when the sector angles are close to 90 deg. Exactly 90 deg is a singular condition for which the major and minor fold angles become decoupled. As the vertex angles move away from 90 deg, though, there grow offsets between the stacked layers, lowering the packing efficiency of the stowed state. Thus, the most efficient structures will generally include many vertices with sector angles close to, but not quite, 90 deg.

There is an inherent tradeoff, though. As one gets closer to the 90 deg singular condition, the geometric advantage between the major and minor fold angles becomes huge and variable across the range of motion. As noted in Eq. (6), it varies between μ and $1/\mu$ across the range of motion, and as we approach the singular condition, μ diverges. So, close to the singular state, at some positions, some of the angles are very weakly coupled to the rest of the mechanism and so can readily flex with small deformations of, e.g., panel bending or play in the hinges. As one moves away from the singular state, major and minor angles are more strongly coupled, but offsets between layers are greater, and stacking efficiency is lessened.

In our structure, Fig. 12 shows that the parameter ε is a measure of how far one is from the singular state for the axial/bend and reverse/bend vertices. For close packing, we would want ε to be small, but that will result in large geometric advantages between the major and minor crossing creases.

The way this relationship played out in the fabricated samples was that while in theory, the slightly polygonal curvature of the axial creases should have been sufficient to force single-DOF motion, in practice, they felt "floppy" due to the weak geometric coupling between the crossed creases.

Evaluation of the tradeoff between stacking efficiency and compliance, mediated by the angle parameter ε, requires consideration of many more factors: residual flexibility of panels, play in hinges, and fabricational inaccuracies, to name a few. Exploration of such tradeoffs is something we defer to the future. We note, however, that some special properties of the constant-height flashers suggest several strategies for adding stiffness in ways that reduce or prevent parasitic flexing modes, as we will mention in our conclusions.

9 Conclusions and Discussion

In conclusion, we have presented a family of flasher mechanisms that possess rigid foldability, thereby making them suitable for the implementation of deployable mechanisms with rigid hinged panels. Many of these mechanisms exhibit single-DOF motion, which is another desirable trait. We presented constructive algorithms for the 2D crease patterns and 3D folded forms and the relevant fold angles of all creases. We presented specific examples with fourfold and sixfold rotational symmetry, but the analysis is fully parameterized on the rotational order m, so that other rotational orders may be readily similarly constructed.

While it is possible to design all of the vertices of a flasher to exhibit kinematic single-DOF motion compatible with the dynamic fold angles of all other interior vertices, it is not possible to achieve such consistency around the central polygon as well. Consistency may be restored by cutting the pattern radially and removing the central polygon. The result is a true single-DOF kinematic mechanism, however, at the cost of breaking the radial symmetry and potentially complicating its implementation.

A common usage configuration for a flasher-based deployable is to wrap the mechanism around a central payload in the stowed state (e.g., Refs. [3] and [8]), and then deploy it to a disk around the payload in the deployed state. The cut flasher still supports

this mode of deployment, as the stowed and deployed states are identical to those of an uncut flasher. However, the cut flasher would only be solidly fixed along a single edge of the central polygon, as the other edges will move away from the central hub, then come back into contact over the course of the deployment motion. This would entail greater mechanical complexity, but would allow such flashers to be used in applications where the thickness and stiffness of the panels must be accommodated in design, e.g., solar arrays.

We speculate that, instead of introducing a radial cut, a single-DOF mechanism may be achievable by further triangulation of some or all of the quadrilateral panels with further hinges. Indeed, it is clear from observation that flashers created from flexible materials and pin hinges incorporate panel flexing as part of their deployment motion. Whether such triangulation can be done "just enough" to create a single DOF is an interesting question and a potential avenue for further exploration.

We also showed how to construct constant-height variants of single-DOF rigidly foldable flashers. The constant-height property provides a more efficient packing of facet panels than flashers in which the reverse fold vertices are aligned with bend vertices; it also allows one to avoid degree-6 vertices that could conceivably give rise to unwanted flexible motions.

The constant-height variants also enable another intriguing possibility. As noted above, in both the flat and stowed forms, all of the vertices of the upper reverse folds lie in the same horizontal plane, and all of the vertices of the bottom reverse folds, including the vertices of the central polygon, also lie in the same horizontal plane. It is readily shown that the coplanarity of these sets of vertices holds throughout the full range of motion from flat to fully stowed. This property, in turn, suggests several interesting avenues for building upon constant-height flashers to create more functional or robust mechanisms. For example, one could connect adjacent sets of panels with scissor-joints to add stiffness against out-of-plane motions, thereby circumventing the unwanted compliance of near-singular vertices noted in Sec. 8.

We note, too, that the planarity of the top and bottom surfaces across the range of motion also supports the concept of stacking flashers to create cellular forms that have overall rotational deployment motions, in analogy with the translational deployment of Tachi-Miura cellular forms [18].

More broadly, we have shown an approach for constructing large-scale single-DOF mechanisms by making use of the unique properties of flat-foldable degree-4 vertices—specifically, the proportionality relationship of Eq. (4). This behavior was noted by Tachi [16], who demonstrated flat-foldable "generalized Miura-ori." As shown here, this property can be used to construct large single-DOF networks that provide useful functionality even when the mechanism is never folded all the way (or even close) to the fully flat state; individual vertex flat-foldability is used simply as a means to attain constancy of $\tan(1/2)\gamma_i/\tan(1/2)\gamma_j$ for every pair $\{i,j\}$ of vertices in the network. We expect that this property can be used to construct many more complex, single-DOF, origami-based mechanisms in the future.

Acknowledgment

This paper is based on the work supported by the National Science Foundation and the Air Force Office of Scientific Research through NSF Grant No. EFRI-ODISSEI-1240417 at the Brigham Young University.

Appendix

Sector-Dihedral Relations

Here, we derive new formulas relating the dihedral angles of a general degree-4 vertex to the values of the surrounding sector angles. A portion of this derivation is also presented in Ref. [19].

We build off of the work of Huffman [13], following his approach and using several of his results. We consider the trace of the vertex on the Gaussian sphere, as shown in Fig. 22 (analogous to Fig. 3 of Ref. [13]). The Gaussian sphere is a dual-space representation of the vertex and is the path traced out on a unit sphere by the surface normal vector as it travels around the vertex. The flat sectors of the vertex, being planar, map to points on the trace. We denote by $\{a_i\}$ the points on the trace, which correspond to sectors with sector angles $\{\alpha_i\}$. Since the normal vector sweeps out an arc at each fold, the dihedral angles (fold angles) of the vertex map to arcs on the Gaussian sphere.

As noted by Huffman, the trace of a developable degree-4 vertex always takes the general form of a (not necessarily symmetric) bow-tie, and the solid angles subtended by the two triangles of the bow are equal (this follows directly from developability of the vertex).

Huffman derived relations between opposite dihedral angles for a general vertex (Eqs. (2*a*)–(2*c*) in Ref. [13]). Using our notation, they are

$$\frac{\sin^2\left(\frac{1}{2}\gamma_2\right)}{\sin^2\left(\frac{1}{2}\gamma_4\right)} = \frac{\sin\alpha_3\sin\alpha_4}{\sin\alpha_1\sin\alpha_2} \tag{A1}$$

and

$$\frac{\sin^2\left(\frac{1}{2}\gamma_1\right)}{\sin^2\left(\frac{1}{2}\gamma_3\right)} = \frac{\sin\alpha_2\sin\alpha_3}{\sin\alpha_1\sin\alpha_4} \tag{A2}$$

For a flat-foldable vertex ($\alpha_1+\alpha_3=\pi$ and $\alpha_2+\alpha_4=\pi$) with crease assignment as shown in Fig. 22, these simplify to

$$\gamma_2=\gamma_4,\ \gamma_1=-\gamma_3 \tag{A3}$$

Huffman also derived a relationship between adjacent dihedral angles (Eq. (3) in Ref. [13]); here, we derive one that is somewhat simpler.

We consider the four triangles on the Gaussian sphere

$$\triangle(a_4,a_1,a_2),\ \triangle(a_4,a_3,a_2),\ \triangle(a_1,a_4,a_3),\ \text{and}\ \triangle(a_1,a_2,a_3)$$

each composed of two of the smaller lettered triangles in Fig. 22.

Because the first two of the four share the triangle F and the two halves of the bow-tie of the trace have equal area, the first pair of triangles has equal area, as do the second pair

$$\text{area}\left(\triangle(a_4,a_1,a_2)\right)=\text{area}\left(\triangle(a_4,a_3,a_2)\right)=E+F \tag{A4}$$

$$\text{area}\left(\triangle(a_1,a_4,a_3)\right)=\text{area}\left(\triangle(a_1,a_2,a_3)\right)=E+G \tag{A5}$$

Using a cotangent formula for triangle areas from Ref. [13] (see unmarked equation preceding Eq. (1) in Ref. [13]), we can establish an equality for each pair of triangles

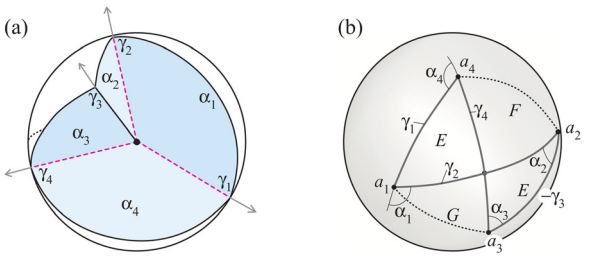

Fig. 22 Schematic of a degree-4 vertex. (*a*) The vertex embedded in a unit sphere. Dashed lines are valley folds, and dotted lines are mountain folds. (*b*) The trace of the vertex on the Gaussian sphere. Since γ_3 is a mountain fold, its sign is negative.

$$\cot\left(\frac{1}{2}\gamma_1\right)\cot\left(\frac{1}{2}\gamma_2\right)\csc(\pi-\alpha_1)+\cot(\pi-\alpha_1)$$
$$=\cot\left(\frac{1}{2}\gamma_4\right)\cot\left(-\frac{1}{2}\gamma_3\right)\csc\alpha_3+\cot\alpha_3 \tag{A6}$$

$$\cot\left(\frac{1}{2}\gamma_1\right)\cot\left(\frac{1}{2}\gamma_4\right)\csc(\pi-\alpha_4)+\cot(\pi-\alpha_4)$$
$$=\cot\left(\frac{1}{2}\gamma_2\right)\cot\left(-\frac{1}{2}\gamma_3\right)\csc\alpha_2+\cot\alpha_2 \tag{A7}$$

Now, we can eliminate one of the half-angle cotangents from these two equations and solve for any one of the four in terms of the two remaining. For example,

$$\cot\left(\frac{1}{2}\gamma_2\right)=\frac{\cot\left(\frac{1}{2}\gamma_3\right)(\cot\alpha_2+\cot\alpha_4)\csc\alpha_3-\cot\left(\frac{1}{2}\gamma_1\right)(\cot\alpha_1+\cot\alpha_3)\csc\alpha_4}{\cot^2\left(\frac{1}{2}\gamma_3\right)\csc\alpha_2\csc\alpha_3-\cot^2\left(\frac{1}{2}\gamma_1\right)\csc\alpha_1\csc\alpha_4} \tag{A8}$$

But this can be simplified; by using Eq. (A2), the denominator simplifies to

$$\cot^2\left(\frac{1}{2}\gamma_3\right)\csc\alpha_2\csc\alpha_3-\cot^2\left(\frac{1}{2}\gamma_1\right)\csc\alpha_1\csc\alpha_4$$
$$=\csc\alpha_1\csc\alpha_4-\csc\alpha_2\csc\alpha_3 \tag{A9}$$

Applying this and corresponding relations for all four half-angle cotangents, we find linear relationships among the four

$$\cot\left(\frac{1}{2}\gamma_1\right)=\frac{\cot\left(\frac{1}{2}\gamma_2\right)(\cot\alpha_1+\cot\alpha_3)\csc\alpha_2-\cot\left(\frac{1}{2}\gamma_4\right)(\cot\alpha_2+\cot\alpha_4)\csc\alpha_3}{\csc\alpha_3\csc\alpha_4-\csc\alpha_1\csc\alpha_2} \tag{A10}$$

$$\cot\left(\frac{1}{2}\gamma_2\right)=\frac{\cot\left(\frac{1}{2}\gamma_3\right)(\cot\alpha_2+\cot\alpha_4)\csc\alpha_3-\cot\left(\frac{1}{2}\gamma_1\right)(\cot\alpha_1+\cot\alpha_3)\csc\alpha_4}{\csc\alpha_1\csc\alpha_4-\csc\alpha_2\csc\alpha_3} \tag{A11}$$

$$\cot\left(\frac{1}{2}\gamma_3\right)=\frac{\cot\left(\frac{1}{2}\gamma_2\right)(\cot\alpha_2+\cot\alpha_4)\csc\alpha_1-\cot\left(\frac{1}{2}\gamma_4\right)(\cot\alpha_1+\cot\alpha_3)\csc\alpha_4}{\csc\alpha_3\csc\alpha_4-\csc\alpha_1\csc\alpha_2} \tag{A12}$$

$$\cot\left(\frac{1}{2}\gamma_4\right)=\frac{\cot\left(\frac{1}{2}\gamma_3\right)(\cot\alpha_1+\cot\alpha_3)\csc\alpha_2-\cot\left(\frac{1}{2}\gamma_1\right)(\cot\alpha_2+\cot\alpha_4)\csc\alpha_1}{\csc\alpha_1\csc\alpha_4-\csc\alpha_2\csc\alpha_3} \tag{A13}$$

Now, each of Eqs. (A2) and (A3) may be rewritten in terms of cotangents

$$\cot^2\left(\frac{1}{2}\gamma_2\right)=\csc^2\left(\frac{1}{2}\gamma_4\right)\frac{\sin\alpha_1\sin\alpha_2}{\sin\alpha_3\sin\alpha_4}-1$$
$$=\left(1+\cot^2\left(\frac{1}{2}\gamma_4\right)\right)\frac{\sin\alpha_1\sin\alpha_2}{\sin\alpha_3\sin\alpha_4}-1 \tag{A14}$$

$$\cot^2\left(\frac{1}{2}\gamma_4\right)=\csc^2\left(\frac{1}{2}\gamma_2\right)\frac{\sin\alpha_3\sin\alpha_4}{\sin\alpha_1\sin\alpha_2}-1$$
$$=\left(1+\cot^2\left(\frac{1}{2}\gamma_2\right)\right)\frac{\sin\alpha_3\sin\alpha_4}{\sin\alpha_1\sin\alpha_2}-1 \tag{A15}$$

$$\cot^2\left(\frac{1}{2}\gamma_1\right)=\csc^2\left(\frac{1}{2}\gamma_3\right)\frac{\sin\alpha_1\sin\alpha_4}{\sin\alpha_2\sin\alpha_3}-1$$
$$=\left(1+\cot^2\left(\frac{1}{2}\gamma_3\right)\right)\frac{\sin\alpha_1\sin\alpha_4}{\sin\alpha_2\sin\alpha_3}-1 \tag{A16}$$

$$\cot^2\left(\frac{1}{2}\gamma_3\right)=\csc^2\left(\frac{1}{2}\gamma_1\right)\frac{\sin\alpha_2\sin\alpha_3}{\sin\alpha_1\sin\alpha_4}-1$$
$$=\left(1+\cot^2\left(\frac{1}{2}\gamma_1\right)\right)\frac{\sin\alpha_2\sin\alpha_3}{\sin\alpha_1\sin\alpha_4}-1 \tag{A17}$$

Recall that for the two pairs of opposite angles, one pair must have the same sign and the other must have the opposite sign. When we take square roots of Eqs. (A14) and (A16), we must choose signs that respect this convention. We can denote the possible choices by introducing operations $\pm_i$, where the sign of each is chosen to match the desired crease directions. Then, we have that

$$\cot\left(\frac{1}{2}\gamma_2\right)=\pm_2\sqrt{\left(1+\cot^2\left(\frac{1}{2}\gamma_4\right)\right)\frac{\sin\alpha_1\sin\alpha_2}{\sin\alpha_3\sin\alpha_4}-1} \tag{A18}$$

$$\cot\left(\frac{1}{2}\gamma_4\right)=\pm_4\sqrt{\left(1+\cot^2\left(\frac{1}{2}\gamma_2\right)\right)\frac{\sin\alpha_3\sin\alpha_4}{\sin\alpha_1\sin\alpha_2}-1} \tag{A19}$$

$$\cot\left(\frac{1}{2}\gamma_1\right)=\pm_1\sqrt{\left(1+\cot^2\left(\frac{1}{2}\gamma_3\right)\right)\frac{\sin\alpha_1\sin\alpha_4}{\sin\alpha_2\sin\alpha_3}-1} \tag{A20}$$

$$\cot\left(\frac{1}{2}\gamma_3\right)=\pm_3\sqrt{\left(1+\cot^2\left(\frac{1}{2}\gamma_1\right)\right)\frac{\sin\alpha_2\sin\alpha_3}{\sin\alpha_1\sin\alpha_4}-1} \tag{A21}$$

and each of these may be substituted into the proceeding four equations to give a one-to-one relationship between any dihedral angle and either of its immediately adjacent angles. We summarize these for the general case and for the specific cases of straight-major, straight-minor, and flat-foldable, where the relationships take on somewhat simpler forms.

From Minor Dihedral.

Consider first a minor pair, where γ_1 is the known angle. Then, from Eq. (A2), the other minor angle is given by

$$\gamma_3=-2\sin^{-1}\left[\sin\left(\frac{1}{2}\gamma_1\right)\sqrt{\frac{\sin\alpha_1\sin\alpha_4}{\sin\alpha_2\sin\alpha_3}}\right] \tag{A22}$$

which is valid for either sign of γ_1.

The two major angles are then given by

$$\gamma_2=2\cot^{-1}\left[\frac{\cot\left(\frac{1}{2}\gamma_3\right)(\cot\alpha_2+\cot\alpha_4)\csc\alpha_3-\cot\left(\frac{1}{2}\gamma_1\right)(\cot\alpha_1+\cot\alpha_3)\csc\alpha_2}{\csc\alpha_1\csc\alpha_4-\csc\alpha_2\csc\alpha_3}\right] \tag{A23}$$

$$\gamma_4 = 2\cot^{-1}\left[\frac{\cot\left(\frac{1}{2}\gamma_3\right)(\cot\alpha_1+\cot\alpha_3)\csc\alpha_2 - \cot\left(\frac{1}{2}\gamma_1\right)(\cot\alpha_2+\cot\alpha_4)\csc\alpha_1}{\csc\alpha_1\csc\alpha_4 - \csc\alpha_2\csc\alpha_3}\right] \tag{A24}$$

These two expressions give the proper signs for γ_2 and γ_4 for all possible sets of valid sector angles and given angle γ_1, except for the special cases where the two expressions are undetermined: flat-foldable, straight-minor, and straight-major.

For the flat-foldable special case, where $\alpha_1+\alpha_3=\pi$ and $\alpha_2+\alpha_4=\pi$, we have

$$\gamma_3 = -\gamma_1 \tag{A25}$$

$$\begin{aligned}\gamma_2 = \gamma_4 &= 2\cot^{-1}\left[\cot\left(\frac{1}{2}\gamma_1\right)\frac{\sin\frac{1}{2}(\alpha_1-\alpha_2)}{\sin\frac{1}{2}(\alpha_1+\alpha_2)}\right] \\ &= 2\cot^{-1}\left[\mu^{-1}\cot\left(\frac{1}{2}\gamma_1\right)\right]\end{aligned} \tag{A26}$$

where we have included the fold angle multiplier μ that we introduced above. These equations, too, give the proper sign for all possible sets of sector angles and γ_1.

For the straight-minor special case, where $\alpha_1+\alpha_2=\pi$ and $\alpha_3+\alpha_4=\pi$, we have

$$\gamma_3 = -\gamma_1 \tag{A27}$$

$$\gamma_2 = 2\cot^{-1}\left[\frac{\left(1-\cot^2\left(\frac{1}{2}\gamma_1\right)\right)\cot\alpha_1 + \left(1+\cot^2\left(\frac{1}{2}\gamma_1\right)\right)\cot\alpha_3}{2\cot\left(\frac{1}{2}\gamma_1\right)\csc\alpha_1}\right] \tag{A28}$$

$$\gamma_4 = -2\cot^{-1}\left[\frac{\left(1-\cot^2\left(\frac{1}{2}\gamma_1\right)\right)\cot\alpha_3 + \left(1+\cot^2\left(\frac{1}{2}\gamma_1\right)\right)\cot\alpha_1}{2\cot\left(\frac{1}{2}\gamma_1\right)\csc\alpha_3}\right] \tag{A29}$$

And finally, for the straight-major special case, where $\alpha_1+\alpha_4=\pi$ and $\alpha_2+\alpha_3=\pi$, we have

$$\gamma_3 = -\gamma_1 \tag{A30}$$

$$\gamma_2 = \gamma_4 = \begin{cases}\pm\pi & \text{if } \gamma_1 \neq 0 \\ \text{unspecified} & \text{if } \gamma_1 = 0\end{cases} \tag{A31}$$

From Major Dihedral

Instead of being given a minor dihedral angle, we might instead be given a major dihedral angle, e.g., γ_4. From this, we can calculate the other three dihedrals. For the general case, the other major angle comes from Eq. (A1), given by

$$\gamma_2 = 2\sin^{-1}\left[\sin\left(\frac{1}{2}\gamma_4\right)\sqrt{\frac{\sin\alpha_3\sin\alpha_4}{\sin\alpha_1\sin\alpha_2}}\right] \tag{A32}$$

The two minor angles are then given by

$$\gamma_1 = 2\cot^{-1}\left[\frac{\cot\left(\frac{1}{2}\gamma_2\right)(\cot\alpha_1+\cot\alpha_3)\csc\alpha_2 - \cot\left(\frac{1}{2}\gamma_4\right)(\cot\alpha_2+\cot\alpha_4)\csc\alpha_3}{\csc\alpha_3\csc\alpha_4 - \csc\alpha_2\csc\alpha_1}\right] \tag{A33}$$

$$\gamma_3 = 2\cot^{-1}\left[\frac{\cot\left(\frac{1}{2}\gamma_2\right)(\cot\alpha_2+\cot\alpha_4)\csc\alpha_1 - \cot\left(\frac{1}{2}\gamma_4\right)(\cot\alpha_1+\cot\alpha_3)\csc\alpha_4}{\csc\alpha_3\csc\alpha_4 - \csc\alpha_1\csc\alpha_2}\right] \tag{A34}$$

For the flat-foldable special case, where $\alpha_1+\alpha_3=\pi$ and $\alpha_2+\alpha_4=\pi$, we have

$$\gamma_2 = \gamma_4 \tag{A35}$$

$$\begin{aligned}\gamma_1 = -\gamma_3 &= 2\cot^{-1}\left[\cot\left(\frac{1}{2}\gamma_4\right)\frac{\sin\frac{1}{2}(\alpha_1+\alpha_2)}{\sin\frac{1}{2}(\alpha_1-\alpha_2)}\right] \\ &= 2\cot^{-1}\left[\mu\cot\left(\frac{1}{2}\gamma_4\right)\right]\end{aligned} \tag{A36}$$

For the straight-minor special case, where $\alpha_1+\alpha_2=\pi$ and $\alpha_3+\alpha_4=\pi$, we have

$$\gamma_2 = 2\sin^{-1}\left[\sin\left(\frac{1}{2}\gamma_4\right)\frac{\sin\alpha_3}{\sin\alpha_1}\right] \tag{A37}$$

$$\gamma_1 = -\gamma_3 = 2\cot^{-1}\left[\frac{\left(\cot\left(\frac{1}{2}\gamma_2\right)\csc\alpha_1 + \cot\left(\frac{1}{2}\gamma_4\right)\csc\alpha_4\right)(\cot\alpha_1+\cot\alpha_3)}{\csc^2\alpha_3 - \csc^2\alpha_1}\right] \tag{A38}$$

And last, for the straight-major special case, where $\alpha_1+\alpha_4=\pi$ and $\alpha_2+\alpha_3=\pi$, we have

$$\gamma_2 = \gamma_4 \tag{A39}$$

$$\gamma_1 = -\gamma_3 = \begin{cases}0 & \text{if } \gamma_4 \neq 0 \\ \text{unspecified} & \text{if } \gamma_4 = \pm\pi\end{cases} \tag{A40}$$

Flat-Foldable

The relations between adjacent vertex angles simplify considerably for flat-foldable vertices. From Eq. (A3), $\gamma_2=\gamma_4$, $\gamma_1=-\gamma_3$, and opposite sector angles sum to π, that is, $\alpha_1+\alpha_3=\pi$ and $\alpha_2+\alpha_4=\pi$. In principle, we could substitute these relationships into Eqs. (A10)–(A13), but the expressions become undetermined (zero in both numerator and denominator). Instead, we make the substitution

$$\alpha_3 = \pi - \alpha_1 + \varepsilon, \alpha_4 = \pi - \alpha_2 + \varepsilon \tag{A41}$$

and then take the limit as $\varepsilon \to 0$ using L'Hôpital's rule.

This gives the following result:

$$\frac{\tan\frac{1}{2}\gamma_1}{\tan\frac{1}{2}\gamma_2} = \frac{\sin\left(\frac{1}{2}(\alpha_1-\alpha_2)\right)}{\sin\left(\frac{1}{2}(\alpha_1+\alpha_2)\right)} \tag{A42}$$

This relation not only gives a much simpler formulation than Eqs. (A23), (A24), (A33), and (A34), but it also shows immediately the inequality relationship between major and minor angles. The right side of this expression always has magnitude less than or equal to 1, which means that, except at the endpoints of motion, $|\tan 1/2\gamma_1| < |\tan 1/2\gamma_2|$. And since the tangent function is monotonic, it follows that $|\gamma_{1,3}| < |\gamma_{2,4}|$ over the same range.

For a general vertex, the relationship between adjacent dihedral fold angles is more complex and there is not such a strict inequality between individual pairs of angles. However, we can identify a

similar inequality between *sums* of angles. Because the surface of the Gaussian sphere is a metric space, the triangle inequality holds. With respect to Fig. 22, it follows, then, that:

$$|\gamma_1| + |\gamma_3| \leq |\gamma_2| + |\gamma_4| \tag{A43}$$

with, again, strict inequality holding at all configurations except for the fully open and fully closed states, where the two sides are indeed equal.

References

[1] Lang, R. J., 1997, *Origami in Action*, St. Martin's Griffin, New York.
[2] Kawasaki, T., 2005, *Roses, Origami, & Math*, Japan Publications Trading, Tokyo.
[3] Guest, S. D., and Pellegrino, S., 1992, "Inextensional Wrapping of Flat Membranes," First International Seminar on Structural Morphology, Montpellier, France, Sept. 7–11, pp. 203–215.
[4] Nojima, T., 2002, "Origami Modeling of Functional Structures Based on Organic Patterns," Master's thesis, Graduate School of Kyoto University, Kyoto, Japan.
[5] Reynolds, W. D., Jeon, S. K., Banik, J. A., and Murphey, T. W., 2014, "Advanced Folded Approaches for Deployable Spacecraft Payloads," ASME Paper No. DETC2013-13378.
[6] Natori, M. C., Katsumata, N., Yamakawa, H., Sakamoto, H., and Kishimoto, N., 2014, "Conceptual Model Study Using Origami for Membrane Space Structures," ASME Paper No. DETC2013-13490.
[7] Guest, S. D., and Pellegrino, S., 1996, "A New Concept for Solid Surface Deployable Antennas," Acta Astronaut., **38**(2), pp. 103–113.
[8] Zirbel, S. A., Lang, R. J., Thomson, M. W., Sigel, D. A., Walkemeyer, P. E., Trease, B. P., Magleby, S. P., and Howell, L. L., 2013, "Accommodating Thickness in Origami-Based Deployable Arrays," ASME J. Mech. Des., **135**(11), p. 111005.
[9] Tachi, T., 2011, "Rigid-Foldable Thick Origami," *Origami*^{5}, CRC Press, Boca Raton, FL, pp. 253–264.
[10] Edmonson, B. J., Lang, R. J., Magleby, S. P., and Howell, L. L., 2014, "An Offset Panel Technique for Thick Rigidly Foldable Origami," ASME Paper No. DETC2014-35606.
[11] Miura, K., 2009, "The Science of Miura-ori: A Review," *Origami*^{4}, R. J. Lang, ed., A K Peters, Natick, MA, pp. 87–100.
[12] Scheel, H., 1974, "Space-Saving Storage of Flexible Sheets," U.S. Patent No. 3,848,821.
[13] Huffman, D. A., 1976, "Curvature and Creases: A Primer on Paper," IEEE Trans. Comput., **C-25**(10), pp. 1010–1019.
[14] Kawasaki, T., 1989, "On the Relation Between Mountain-Creases and Valley-Creases of a Flat Origami," First International Meeting of Origami Science and Technology, Ferrara, Italy, Dec. 6–7, H. Huzita, ed., pp. 229–237.
[15] Hull, T., 2006, *Project Origami*, A K Peters, Natick, MA.
[16] Tachi, T., 2009, "Generalization of Rigid Foldable Quadrilateral Mesh Origami," 50th Symposium of the International Association for Shell and Spatial Structures, Valencia, Spain, Sept. 28–Oct. 2.
[17] Tibbalds, B., Guest, S. D., and Pellegrino, S., 2004, "Inextensional Packaging of Thin Shell Slit Reflectors," Tech. Mech., **24**(3–4), pp. 211–220.
[18] Tachi, T., and Miura, K., 2012, "Rigid-Foldable Cylinders and Cells," J. Int. Assoc. Shell Spat. Struct. (IASS), **53**(4), pp. 217–226.
[19] Wilcox, E. W., Shrager, A., Bowen, L., Frecker, M., von Lockette, P., Simpson, T., Magleby, S. P., Lang, R. J., and Howell, L. L., 2015, "Considering Mechanical Advantage in the Design and Actuation of an Origami-Based Mechanisms," ASME Paper No. DETC2015-47708.